Science Advances
AAAS

advances.sciencemag.org/cgi/content/full/6/19/eaba5337/DC1

Supplementary Materials for

Magnetic field–driven assembly and reconfiguration of multicomponent supraparticles

A. Al Harraq, J. G. Lee, B. Bharti*

*Corresponding author. Email: bbharti@lsu.edu

Published 8 May 2020, *Sci. Adv.* **6**, eaba5337 (2020)
DOI: 10.1126/sciadv.aba5337

The PDF file includes:

Figs. S1 to S14
Notes S1 to S4
Legend for movies S1 to S7

Other Supplementary Material for this manuscript includes the following:

(available at advances.sciencemag.org/cgi/content/full/6/19/eaba5337/DC1)

Movies S1 to S7

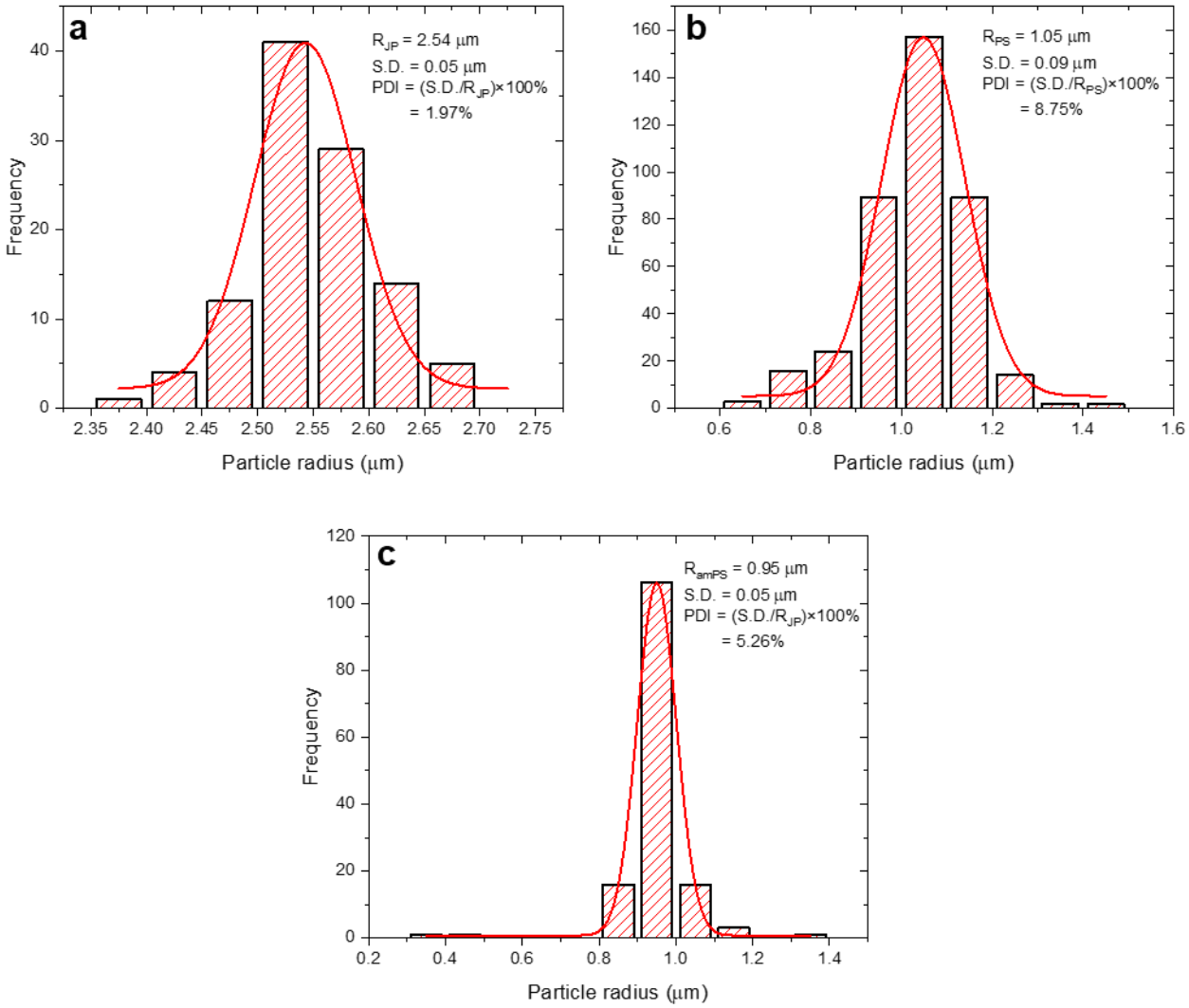

fig. S1. Particle size distributions using light microscopy. (a) 5.1 μm in diameter, red fluorescent, carboxylated polystyrene microspheres (Magsphere Inc.), **(b)** 2.0 μm in diameter, green fluorescent, carboxylated polystyrene microspheres (Magsphere Inc.) and **(c)** 1.94 μm in diameter, green fluorescent, aminated polystyrene microspheres (Magsphere Inc.).

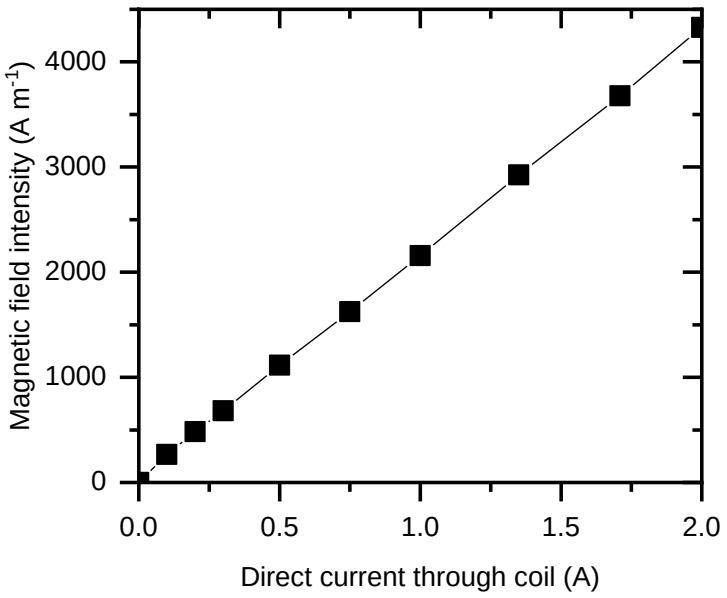

fig. S2. Current/mag. field calibration curve for electromagnetic coil. Manipulation of the applied magnetic field is done by tuning the current flowing through the Helmholtz coil using a DC generator. The equivalent magnetic field is obtained via a handheld magnetometer.

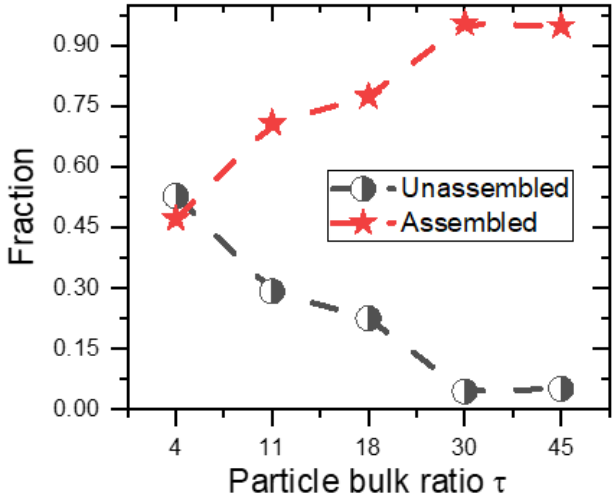

fig. S3. Fraction of assembled structures and unassembled Janus particles. Increasing the particle bulk ratio τ drastically increases the fraction of core patchy particles which are assembled with satellites to form supraparticles. At $\tau = 4$, about 0.55 patchy particles are left unassembled at equilibrium; at $\tau = 45$, only 0.05 of them is unassembled.

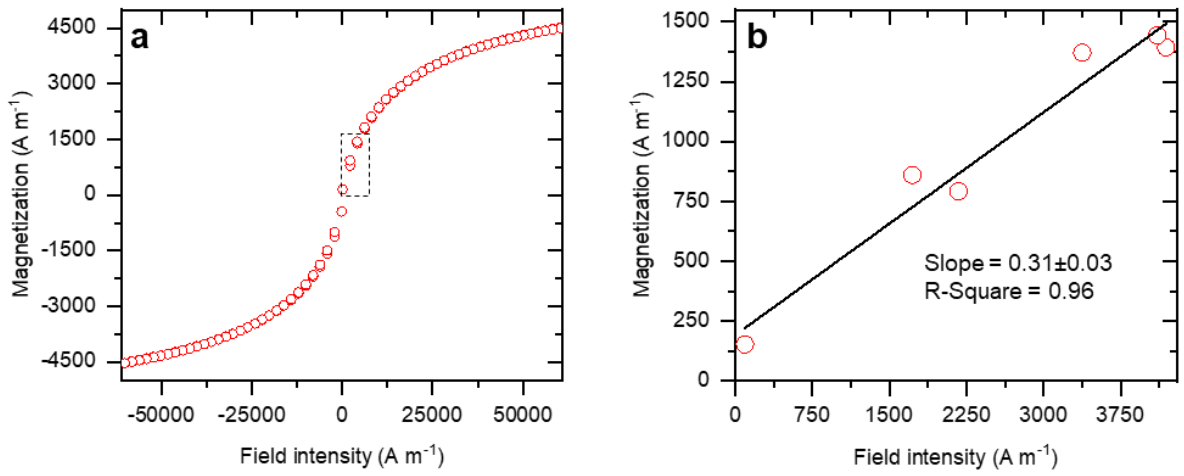

fig. S4. SQUID measurements of ferrofluid stock (2.3 vol. %). (a) Field vs magnetization curve for ferrofluid. The dotted box encloses the linear region of interest. **(b)** Linear fit on SQUID data revealing magnetic susceptibility from the slope: $\chi_{FF} = 0.31$.

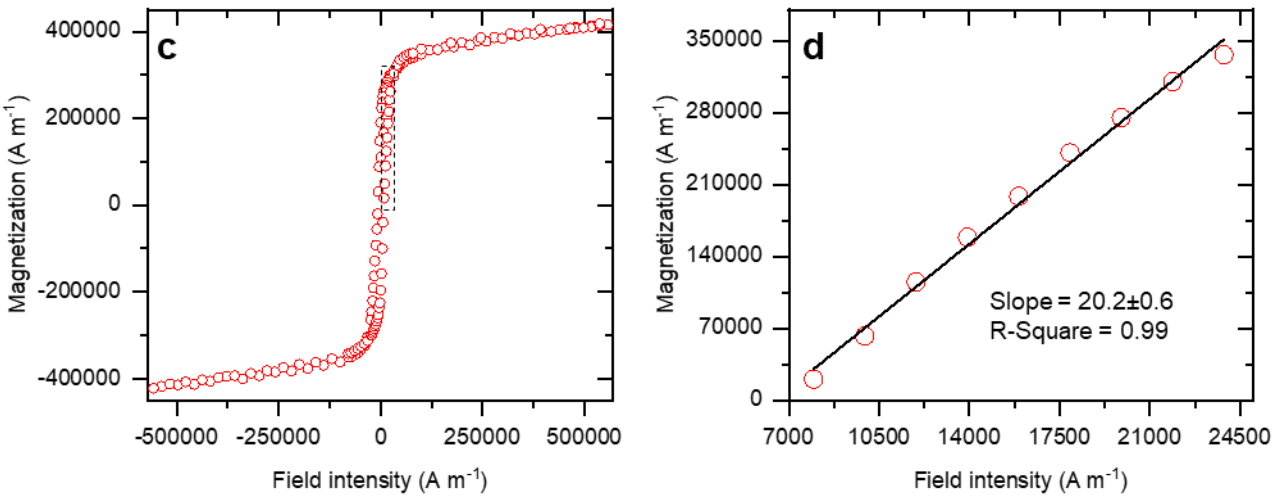

fig. S5. SQUID measurements of iron-patched particles. (a) Field vs magnetization curve for Janus particle. The dotted box encloses the linear region of interest. The selection is justified by the minimal coercivity of the thin iron layer, which behaves as a soft ferromagnet with nearly anhysteretic magnetization. **(b)** Linear fit on SQUID data revealing magnetic susceptibility from the slope: $\chi_{Fe} = 20.2$.

note S1. Determination of magnetic permeability of thin iron shell.

The magnetic permeability of the iron patch (μ_P) is determined via the method outlined by T.B. Jones *(35)* for spherical shells.

$$\mu_P = \mu_{Fe}\left\{\frac{a^3 + 2\left(\frac{\mu_v - \mu_{Fe}}{\mu_0 + 2\mu_{Fe}}\right)}{a^3 - \left(\frac{\mu_v - \mu_{Fe}}{\mu_v + 2\mu_{Fe}}\right)}\right\} = 1.49$$

where $\mu_{Fe} = \chi_{Fe} + 1 = 21.2$ and $\mu_v = 1$ is the relative magnetic permeability of free space. The ratio of concentric radii is expressed as $a = \frac{R_C + t}{R_C}$. This calculation approximates the thin metal shell with $\chi_{Fe} = 20.2$ to a full patched hemisphere with $\chi_P = 0.49$.

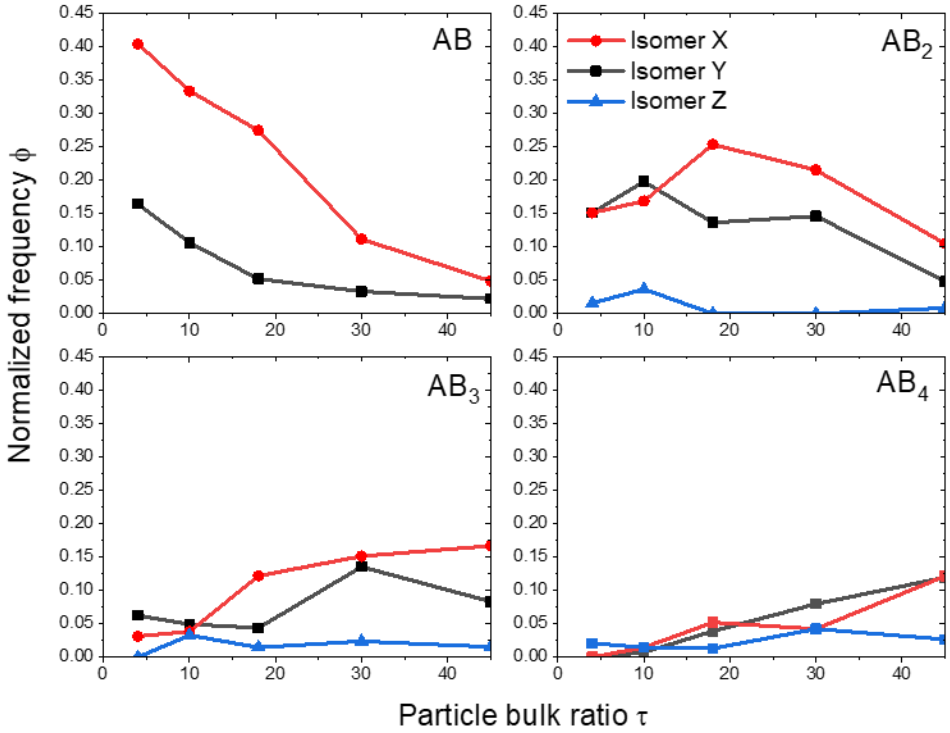

fig. S6. Normalized fractions of isomers X, Y and Z. Frequency of assembly of isomeric supraparticles AB to AB_4 as classified in Fig. 2B. The relative population of X isomers is greater in AB, AB_2 and AB_3 clusters. The absolute number of AB supraparticle is observed to decrease, in accordance with Fig. 2C, and is associated with the increase in population of higher order clusters. The data was obtained by image analysis of ~2800 supraparticle. It should be noted that at values of $\tau < 20$, the relative occurrence of AB_4 supraparticles is too low to be statistically relevant; at values of $\tau > 30$, the experimental data shows a similar trend as lower-order clusters.

note S2. Details on finite element method for magnetostatic interaction energy *(40)*.
Finite element analysis of electromagnetic systems is the solution of Maxwell's equations subject to given boundary conditions, for each subdomain of the system under consideration. Specific to magnetostatics, Maxwell's equations define the fundamental relationship between the magnetic and electric field intensities **H** and **E** and the magnetic and electric flux densities **B** and **D**. The equations are written in differential form as follows:

$$\nabla \times \mathbf{H} = \mathbf{J} + \frac{\delta \mathbf{D}}{\delta t} \qquad \text{Maxwell-Ampère's law}$$

$$\nabla \times \mathbf{E} = -\frac{\delta \mathbf{B}}{\delta t} \qquad \text{Faraday's law}$$

$$\nabla \cdot \mathbf{B} = 0 \qquad \text{Gauss' law}$$

The system of equations is closed by including the constitutive relation describing the macroscopic magnetic properties of the domain. This is $\mathbf{B} = \mu_0(\mathbf{H} + \mathbf{M})$ where μ_0 is the permeability of free space, which is equivalent in SI to $4\pi \times 10^{-7}$H m^{-1}. The magnetization **M** is a vector which may be interpreted as the volume density of magnetic dipole moments. It is directly proportional to the magnetic field by a parameter known as magnetic susceptibility χ, such that $\mathbf{M} = \chi\mathbf{H}$ for linear materials. Therefore, in the range of field **H** in which a material behaves linearly, the constitutive relationship relating its fundamental electromagnetic quantities is:

$$\mathbf{B} = \mu_0(\mathbf{H} + \chi\mathbf{H}) = \mu_0(1 + \chi)\mathbf{H} = \mu_0\mu_r\mathbf{H}$$

where $\mu_r = 1 + \chi$ is defined as the relative permeability of the material.

The total energetics of the colloidal system are calculated as a sum of the magnetic energy in each subdomain. This is given as:

$$W = \frac{1}{2}\int_V \mathbf{H} \cdot \mathbf{B}\, dV = \frac{1}{2}\int_V \mu_0\mu_r\, \mathbf{H^2}\, dV$$

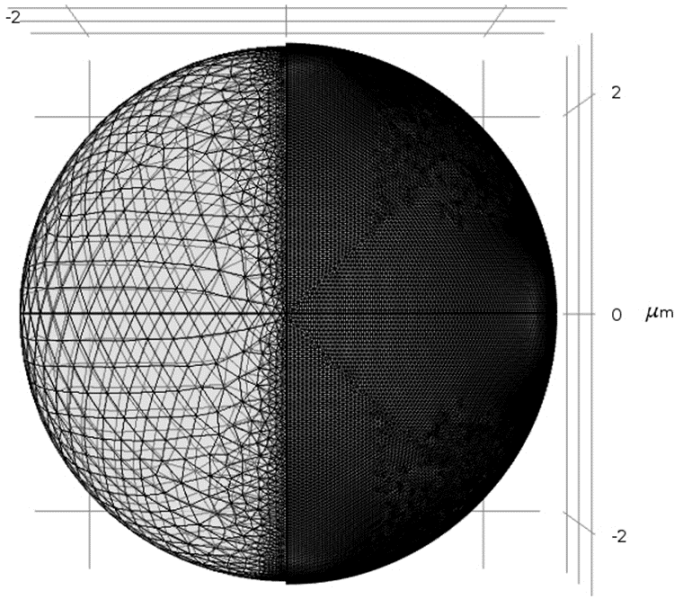

fig. S7. Fine tetrahedral mesh used for finite element analysis. Magnetized domains are divided into small subdomains to perform finite element calculations using COMSOL Multiphysics 5.3. To capture the three-dimensional behavior of the Janus particle under applied magnetic field, a finite tetrahedral mesh is needed. A finer mesh is required for the patch due to its small thickness of 30 nm.

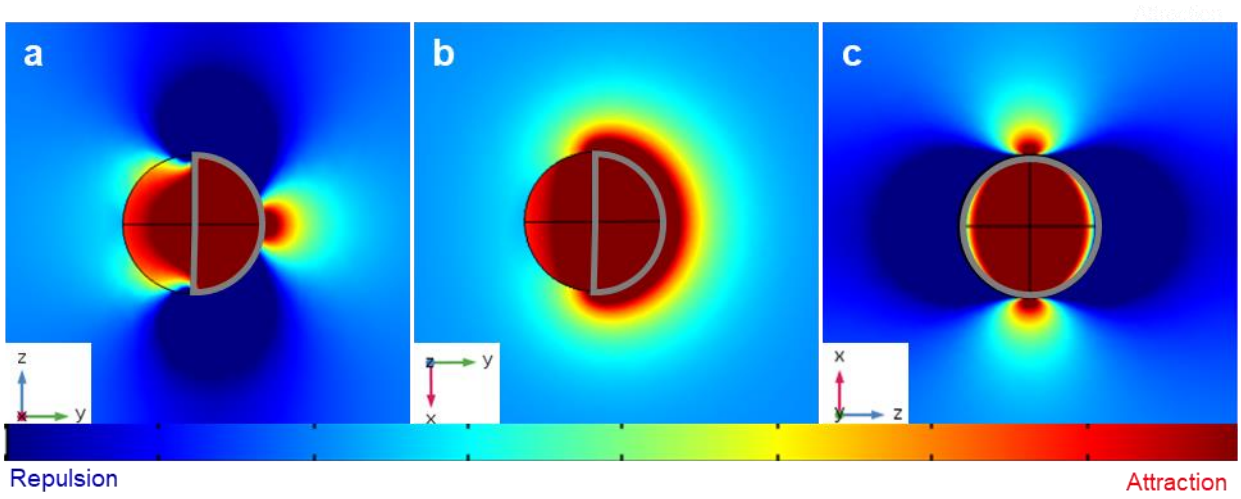

fig. S8. Magnetic flux density obtained via COMSOL. (a) z-y, (b) x-y and (c) x-z slices of magnetic flux density for each of the three dimensions of the simulation. Each 2D slice cuts the Janus particle in half.

note S3. Sample magnetic energy calculation *(35)*.

U_{mag} is obtained by summing the magnetic interaction between patch, satellite and core. As an example, $U_{P\text{-}S}$ for a given angle $\theta = 0^{\circ}$ and constant field intensity $H = 2500$ A m^{-1} is calculated as follows:

- Determine the real part of the Clausius-Mossotti function K_{CM}:

$$K_{CM,P} = \frac{\chi_P - \chi_{FF}}{\chi_P + 2\chi_{FF} + 3} = \frac{0.49 - 0.15}{19.6 + 2 \times 0.585 + 3} = 0.09$$

$$K_{CM,S} = \frac{\chi_S - \chi_{FF}}{\chi_S + 2\chi_{FF} + 3} = \frac{0 - 0.585}{0 + 2 \times 0.585 + 3} = -0.05$$

- Determine domain volumes:

$$V_P = \frac{4}{3}\pi[(R_C + t)^3] \times J = 3.3 \times 10^{-17} m^3$$

$$V_S = \frac{4}{3}\pi R_S^3 = 4.2 \cdot 10^{-18}\ m^3$$

where t is the thickness of the patch

- Calculate moments. Note the linear dependence of moment with patch size J:

$$m_P = V_P\, K_{CM,P}\, H = 7.3 \cdot 10^{-15}\ A\, m^2$$

$$m_S = V_S\, K_{CM,S}\, H = -4.8 \cdot 10^{-16}\ A\, m^2$$

- Calculate the interaction energy with the interparticle distance $r_{P-S} = R_P + R_S$ and convert into kT for T = 300 K:

$$U_{P-S} = \frac{1}{r_{P-S}^3}\left[\mathbf{m_P} \cdot \mathbf{m_S} - 3\frac{(\mathbf{m_P} \cdot \mathbf{r_{P-S}})(\mathbf{m_S} \cdot \mathbf{r_{P-S}})}{r_{P-S}^2}\right] = -53.4\ kT$$

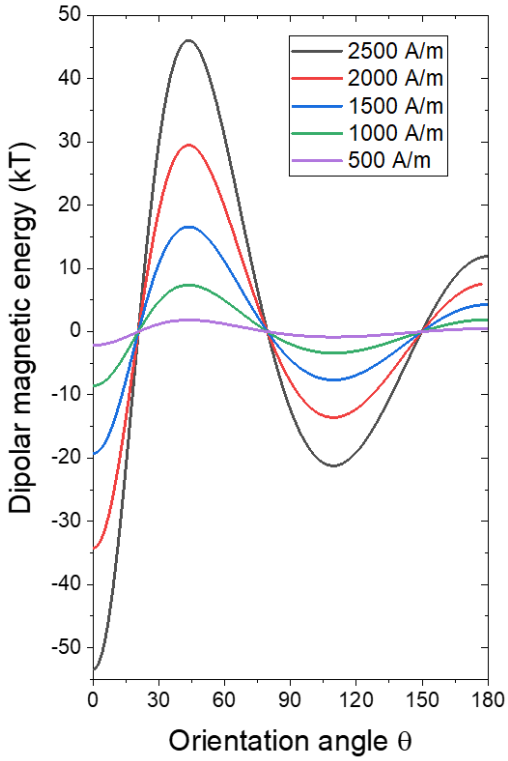

fig. S9. Energy landscape of AB supraparticle as a function of H. Calculated dipolar magnetic energy as a function of orientation angle θ for five values of **H**, going from 2500 A m^{-1} down to 500 A m^{-1}. Decreasing the applied field intensity drastically decreases the energy barrier between metastable states (θ = 109˚) and ground states (θ = 0˚). At **H** = 500 A m^{-1} the energy difference is reduced to ~1.3 kT.

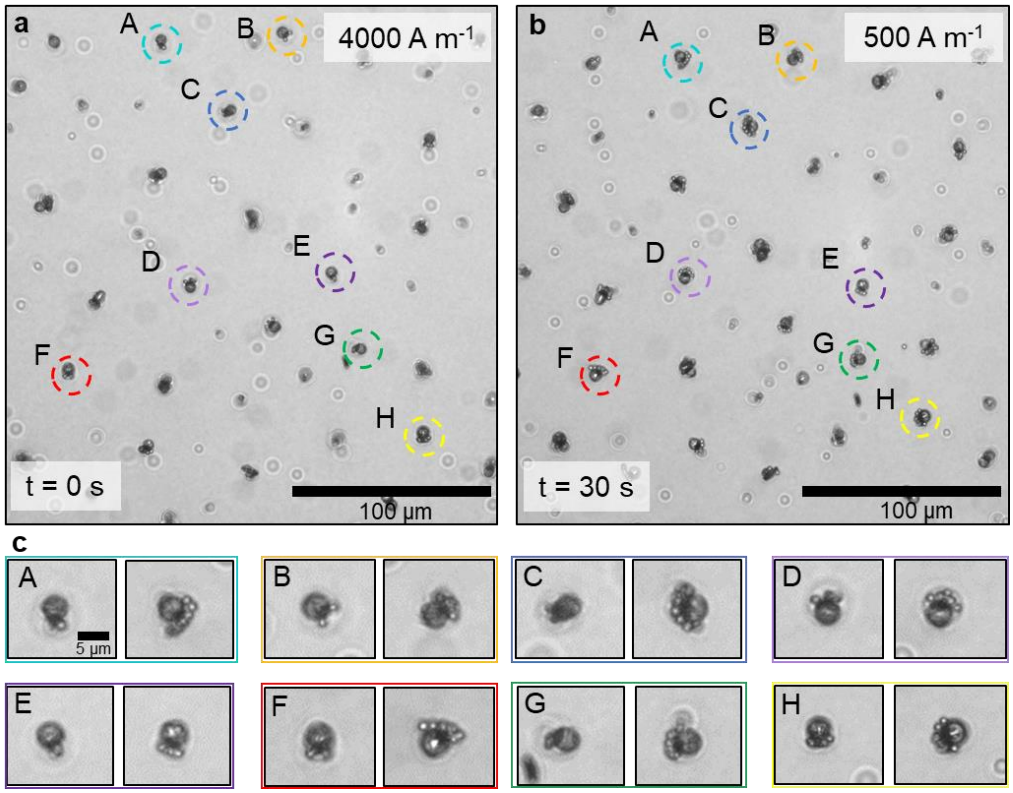

fig. S10. Field-directed supraparticle isomerization. (a) Micrographs of supraparticle obtained at **H** = 4000 A m^{-1} and **(b)** reconfigured supraparticles after lowering field to **H** = 500 A m^{-1} for 30 seconds. **(c)** Collection of supraparticles as seen before and after isomerization.

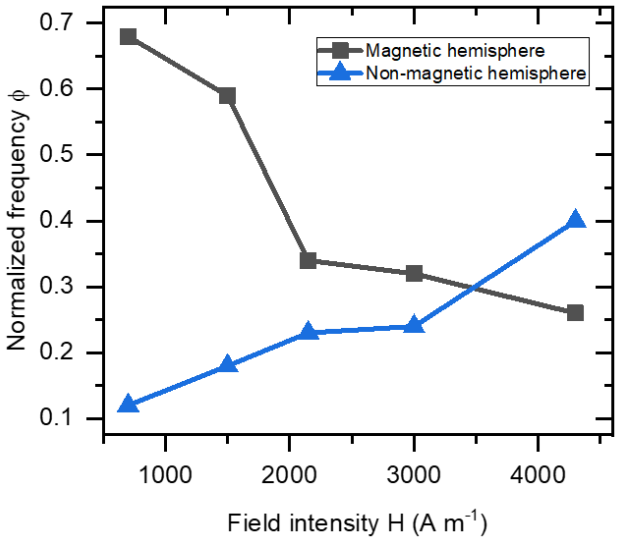

fig. S11. Dependence of preferred attachment site with applied field. Assembly carried out at different field intensity (τ = 10; t = 10 min) leads to different frequency ϕ in metastable state formation. We noted the number of assembled supraparticles with satellites only on the metal patch (gray squares) and only on the non-magnetic hemisphere (blue triangles). Going from 700 to 4300 A m^{-1}, the frequency of metastable states increases as represented by the blue line. Higher energy input allows to kinetically trap satellites onto the less favorable secondary minimum. Lower applied field intensity favors assembly into the more stable state in which satellite particles attach to the iron patch.

note S4. Sample DLVO interaction calculation *(41-44)*.

DLVO interaction energy (U_{DLVO}) was obtained via the summation of Van der Waals (U_{VdW}) and electrostatic (U_{elec}) interactions between two polystyrene particles of radii R_i and R_j, and interparticle distance r_{ij}:

Van der Waals

$$U_{VdW} = -\frac{A}{6r_{ij}}\left(\frac{R_i R_j}{R_i + R_j}\right)$$

- A is the Hamaker constant (J)
- D is the interparticle distance (m)

Electrostatic

$$U_{elec} = \left(\frac{R_i R_j}{R_i + R_j}\right) Z e^{-\kappa r_{ij}}$$

- Z is an interaction constant (N)
- κ is the Debye parameter (m^{-1})

The Hamaker constant is estimated for two polystyrene spheres interacting across water, on the basis of the Lifshitz theory.

$$A = A_{131} = \frac{3\,kT}{4}\left(\frac{\epsilon_1 - \epsilon_3}{\epsilon_1 + \epsilon_3}\right)^2 + \frac{3h\omega}{32\pi\sqrt{2}}\frac{(n_1^2 - n_3^2)^2}{(n_1^2 + n_3^2)^{3/2}}$$

where

- the subscripts 1 and 3 represent respectively polystyrene and water macrophases
- k is the Boltzmann constant (1.38×10^{-23} $m^2 kg\, s^{-2} K^{-1}$)

- T is the temperature (300 K)
- ϵ_r is the relative permittivity ($\epsilon_1 = 2.56$; $\epsilon_2 = 78$)
- h is Planck's constant (6.626×10^{-34} $m^2 kg\, s^{-1}$)
- ω is the main electronic absorption frequency in UV ($3 \times 10^{15} s^{-1}$)
- n is the refractive index ($n_1 = 1.6$; $n_3 = 1.33$)

The electrostatic interaction constant Z in a 1:1 electrolyte solution is determined as follows:

$$Z = 64\pi\epsilon_0\epsilon F\left(\frac{kT}{e}\right)^2 \tanh\left(\frac{e\psi_{0,i}(mV)}{4kT}\right)\tanh\left(\frac{e\psi_{0,j}(mV)}{4kT}\right)$$

- ϵ_0 is the permittivity of free space ($8.85 \times 10^{-12} m^3 kg^{-1} s^4 A^2$)
- ϵ is the permittivity of the medium (78)
- F is a scaling factor due to unknown location of slipping plane (~0.0023)
- e is the elementary charge of an electron ($1.6 \times 10^{-19} C$)
- ψ_0 is the surface potential (estimated as function of ζ-potential in mV using the Gouy-Chapman theory)

The Debye length is estimated to be 18 nm. The Van der Waals and electrostatic contributions are summed to obtain values of DLVO interaction as a function of the interparticle distance r_{ij}. For $r_{ij} = 10$ nm:

at pH 5, $\psi_{0,C} = -75.2$ mV and $\psi_{0,S} = -50.2$ mV

$$U_{DLVO} = U_{VdW} + U_{elec} = -11.4 + 21.1 = 9.7 \text{ a.u.}$$

at pH 2, $\psi_{0,C} = -25.2$ mV and $\psi_{0,S} = 50.7$ mV

$$U_{DLVO} = U_{VdW} + U_{elec} = -11.4 - 21.1 = -32.5 \text{ a.u.}$$

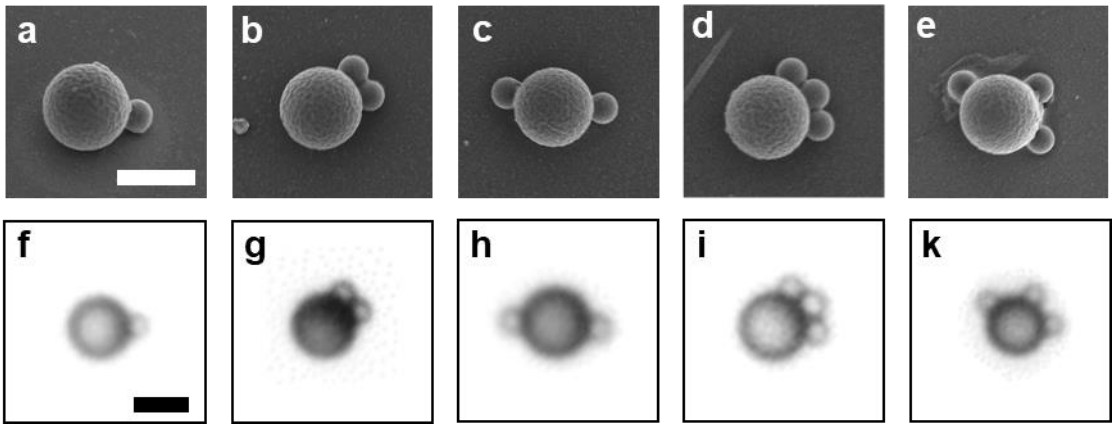

fig. S12. Scanning electron microscopy images of dried supraparticles. (a to e) Scanning electron micrographs of recovered supraparticles obtained from secondary electron detection. **(f to k)** Equivalent brightfield micrographs of supraparticles in their dried states. All scale bars: 5 μm.

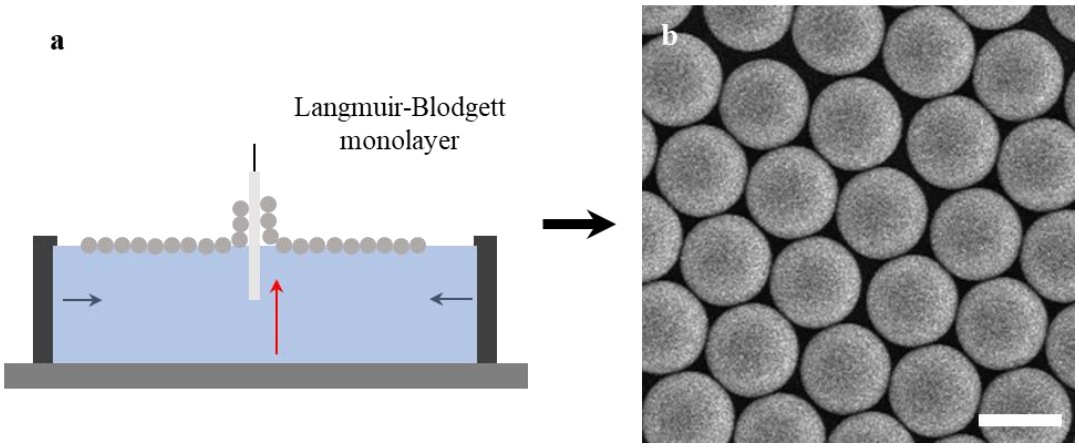

fig. S13. Formation of Langmuir-Blodgett monolayers for fabrication of patchy particles. (a) Schematic of Langmuir-Blodgett technique used to deposit monolayers of particles on glass slides. **(b)** SEM image of obtained monolayer of 5.1 μm polystyrene particles before coating. Scale bar: 5 μm.

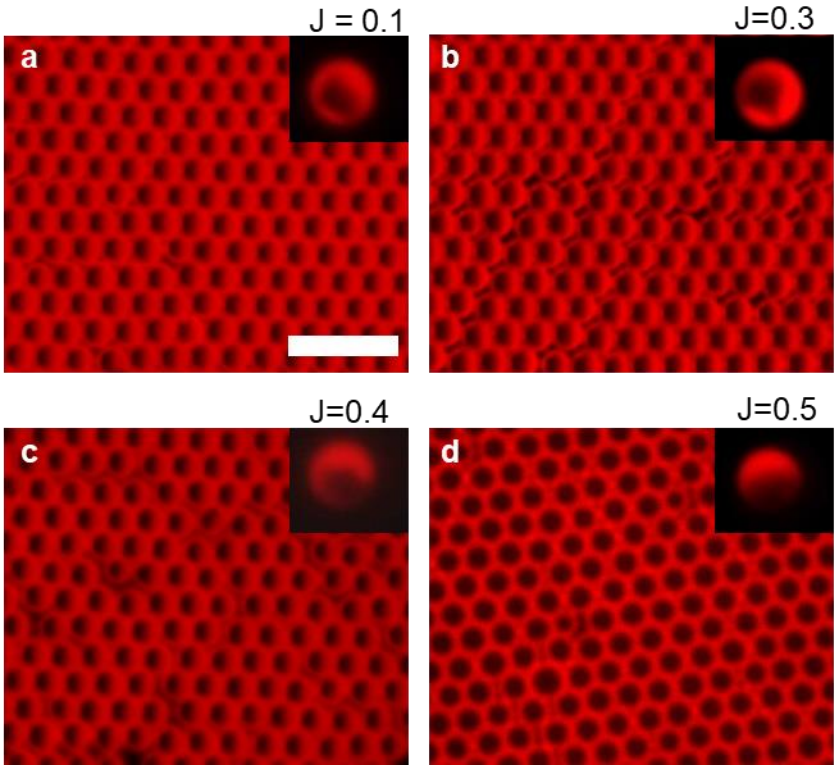

fig. S14. Monolayers of patchy particles of varying J obtained by the method of glancing angle vapor deposition. (a to d) Fluorescence micrographs of particle monolayers following glancing angle deposition of iron obtaining four patch sizes. Insets show a freestanding particle for each patch size. Scale bar: 20 μm.

Movie S1 - Reversibility and dependence of assembly mechanism on ferrofluid.
The assembly of the AB supraparticle occurs only in ferrofluid. Throughout recording, the applied field is toggled on and off to demonstrate the reversibility of the process. The video is divided in two parts: first, the components A and B are found not to assemble in water. In the second part, ferrofluid is the dispersing medium and the supraparticles assemble and disassemble in response to switching external field on and off.

Movie S2 – Multi-step growth of supraparticle from AB to AB_4.
We record the growth of a supraparticle after initial application of magnetic field. The showcased mechanism is the multi-step acquisition of satellites on the patch leading to an AB_4 structure in ~45 seconds.

Movie S3 – Supraparticles assembling and arranging into self-limiting 2D order.
After initiating assembly and forming clusters, the interactions between supraparticles lead to their self-limiting arrangement into a near-equilibrium state.

Movie S4 – Sequence of 2D slices representing magnetic flux intensity calculated via COMSOL.
The data obtained by the finite element calculations is here shown as a sequence of 2D color plots slicing the Janus particle. The coloring of the slices represents the magnetic flux density: the areas in red are more attractive to the non-magnetic satellite. Areas in blue are more repulsive.

Movie S5 – Local spatial orientation leading to isomeric cluster formation.
We record an instance in which differences in the local spatial distribution lead to different isomeric configuration of supraparticle assembled. In the 40 seconds here presented, two core Janus particles attract satellites to form two AB_2 supraparticles. The Janus particle at the top is approached by a satellites from its non-magnetic hemisphere leading to an AB_2 Y structure whereas the structure at the bottom grows into an AB_2 X cluster.

Movie S6 – Supraparticle reconfiguration by lowering applied field intensity.
An AB_6 cluster comprising three satellites on the non-magnetic hemisphere and three on the patch is quickly reconfigured by lowering the intensity of the applied field. The final supraparticle has five satellites on the patch and one on the opposite hemisphere.

Movie S7 – Permanent binding of supraparticles via photo-acid generator.
We showcase the principle of photochemical manipulation of the electrostatic interactions in two parts. The dispersion contains carboxylated core particles, aminated satellites, ferrofluid and a photo-acid generator (diphenyliodonium nitrate). Initially, it is seen that particles assemble when field is applied and disassemble when it is toggled off. After UV light exposure, structures are maintained without the external field. This happens as the surface charge on the aminated satellites is inverted from negative to positive due to photo-acid-induced protonation of the dispersion under UV light.